Post-explosion Evolution of Core-collapse Supernovae

M. Witt[1], A. Psaltis[1] , H. Yasin[1], C. Horn[1], M. Reichert[1,2] , T. Kuroda[3] , M. Obergaulinger[2] , S. M. Couch[4,5,6,7] , and A. Arcones[1,8]

[1] Institut für Kernphysik, Technische Universität Darmstadt, Schlossgartenstr. 2, Darmstadt D-64289, Germany; almudena.arcones@physik.tu-darmstadt.de
[2] Departament d'Astronomia i Astrofísica, Universitat de València, Edifici d'Investigació Jeroni Munyoz, C/ Dr. Moliner, 50, E-46100 Burjassot (València), Spain
[3] Max-Planck-Institut für Gravitationsphysik, Am Mühlenberg 1, D-14476 Potsdam-Golm, Germany
[4] Department of Physics and Astronomy, Michigan State University, East Lansing, MI 48824, USA
[5] Department of Computational Mathematics, Science, and Engineering, Michigan State University, East Lansing, MI 48824, USA
[6] National Superconducting Cyclotron Laboratory, Michigan State University, East Lansing, MI 48824, USA
[7] Joint Institute for Nuclear Astrophysics-Center for the Evolution of the Elements, Michigan State University, East Lansing, MI 48824, USA
[8] GSI Helmholtzzentrum für Schwerionenforschung GmbH, Planckstr. 1, Darmstadt D-64291, Germany
Received 2021 June 22; revised 2021 August 1; accepted 2021 August 2; published 2021 October 27

Abstract

We investigate the post-explosion phase in core-collapse supernovae with 2D hydrodynamical simulations and a simple neutrino treatment. The latter allows us to perform 46 simulations and follow the evolution of the 32 explosion models during several seconds. We present a broad study based on three progenitors (11.2, 15, and 27 $M_\odot$), different neutrino heating efficiencies, and various rotation rates. We show that the first seconds after shock revival determine the final explosion energy, remnant mass, and properties of ejected matter. Our results suggest that a continued mass accretion increases the explosion energy even at late times. We link the late-time mass accretion to initial conditions such as rotation strength and shock deformation at explosion time. Only some of our simulations develop a neutrino-driven wind (NDW) that survives for several seconds. This indicates that NDWs are not a standard feature expected after every successful explosion. Even if our neutrino treatment is simple, we estimate the nucleosynthesis of the exploding models for the 15 $M_\odot$ progenitor after correcting the neutrino energies and luminosities to get a more realistic electron fraction.

Unified Astronomy Thesaurus concepts: Core-collapse supernovae (304); Supernova dynamics (1664); Explosive nucleosynthesis (503); Supernovae (1668)

1. Introduction

Core-collapse supernovae (CCSN) are exciting astrophysical events linked to a broad range of physics, expanding from the explosions themselves to neutrinos and nuclear physics and the high-density equation of state (EOS), including also gravitational waves and nucleosynthesis. Depending on the aspect in focus, different kinds of hydrodynamical simulations are required. Ideally, one would perform 3D, fully general relativistic magneto-hydrodynamic simulations with accurate neutrino transport for many progenitor stars, rotation rates, and magnetic field configurations and strengths, and follow the evolution during several seconds after the explosion. This is clearly computationally impossible today; therefore, some aspects may be sacrificed to gain insights (see, e.g., Janka 2012; Kotake et al. 2012; Müller 2019; Burrows & Vartanyan 2021). Here, we focus on the long-time evolution of several seconds after the explosion and investigate the dynamics, accretion, explosion energy, and approximate nucleosynthesis and their dependency on neutrino heating, rotation, and the progenitor. Therefore, we perform 2D Newtonian simulations with a simple neutrino treatment, namely gray leakage. This allows us to describe and understand important trends occurring during the first seconds after the explosions. However, our simplifications prevent us from making solid quantitative conclusions.

The long-time evolution has been considered in many nucleosynthesis studies of supernova yields. Originally spherically symmetric explosions were artificially triggered by pistons (Woosley & Weaver 1995) or thermal-energy bombs (Thielemann et al. 1996; Nagataki et al. 1998; Nomoto et al. 2006). In the last decades, there have been numerous studies based on spherically symmetric simulations with enhanced neutrino energy deposition (e.g., Scheck et al. 2006; Arcones et al. 2007; O'Connor & Ott 2010; Suwa et al. 2011; Ugliano et al. 2012; Pejcha & Thompson 2015; Perego et al. 2015; Ertl et al. 2016; Müller et al. 2016; Sukhbold et al. 2016; Curtis et al. 2019; Ebinger et al. 2019; Couch et al. 2020; Ebinger et al. 2020). However, there are important multidimensional effects such as convection that impact the nucleosynthesis, explosion energy, explosion morphology (see, e.g., Janka 2012; Kotake et al. 2012; Müller 2019; Nagakura et al. 2019a; Burrows & Vartanyan 2021; Nagakura et al. 2021, and references therein), and neutrino-driven wind (NDW, Arcones & Janka 2011). Recently, it has been possible to perform 2D simulations with good neutrino transport, to follow the evolution for a few seconds after the explosion and to study the supernova nucleosynthesis (see, e.g., Harris et al. 2017; Eichler et al. 2018; Wanajo et al. 2018; Sieverding et al. 2020; Reichert et al. 2021). However, these studies cover a reduced number of models and often only for short times after explosion. Models with longer times usually require a mapping to a larger grid with simpler input physics after shock revival (Wongwathanarat et al. 2015; Müller et al. 2018; Bollig et al. 2021; Stockinger et al. 2020).

Rotation is an additional and important ingredient that affects not only the explosion but also the long-time evolution. The impact of rotation on the explosion has been extensively studied based on 2D (see, e.g., LeBlanc & Wilson 1970; Fryer & Heger 2000; Kotake et al. 2003; Marek & Janka 2009; Suwa et al. 2010; Blondin et al. 2017; Summa et al. 2018; Vartanyan et al. 2018, and references therein) and 3D simulations (Kuroda et al. 2014; Mösta et al. 2014; Nakamura et al. 2014; Takiwaki et al. 2016; Blondin et al. 2017; Summa et al. 2018). In this paper, we also show how rotation impacts the

evolution during the first seconds after the explosion, by affecting the shock morphology and the mass accretion onto the proto-neutron star (PNS).

This paper is organized as follows. In Section 2, we present our simulation setup, initial conditions, and nucleosynthesis network. An overview of the models and their evolution during the first second after bounce is discussed in Section 3. We investigate the long-time evolution in Section 4 including the evolution of the explosion energy (Section 4.1), the impact of rotation and shock deformation (Section 4.2), and the evolution of accretion and NDW (Section 4.3). An estimate of the nucleosynthesis is given in Section 5. We conclude in Section 6.

2. Simulations and Nucleosynthesis

2.1. Hydrodynamics and Neutrinos

We employ the multiphysics FLASH code (Fryxell et al. 2000; Dubey et al. 2009) to perform 2D (cylindrical geometry) CCSN simulations. The domain size for all simulations is 3.2×10^{10} cm along the cylindrical axis and 1.6×10^{10} cm perpendicular to it. Using the adaptive mesh refinement in FLASH (MacNeice et al. 2000), we achieve a maximum resolution of ~488 m. Our setup is similar to previous core-collapse supernova studies with FLASH; see, e.g., Couch & O'Connor (2014) and Couch & Ott (2015). Self-gravity is calculated with a multipole approximation (Couch et al. 2013) of Poisson's equation, without the effective general relativistic potential that was used in O'Connor & Couch (2018). The effective potential leads to more compact PNSs and thus to higher neutrino energies. However, we can neglect these corrections because our simplification in the neutrino transport has a much larger impact on the explosion and nucleosynthesis than does the correction of the gravitational potential. More-over, the relativistic correction may produce a nonconservation of momentum that accumulates for long-time simulations.

Before bounce, the deleptonization scheme of Liebendörfer (2005) is used. After bounce, neutrinos are described by a gray, three-flavor neutrino leakage scheme with a ray-by-ray approximation, as in O'Connor & Ott (2010) and Couch & O'Connor (2014). In order to facilitate the explosions, the neutrino heating is artificially enhanced by a factor, f_{heat}, that was introduced in previous studies (O'Connor & Ott 2010; Couch & O'Connor 2014; Couch & Ott 2015). Here, we adjust slightly the implementation to have the enhanced heating only in the gain layer and until the shock has reached a radius of 1000 km.

Leakage schemes are not as accurate as the more sophisticated neutrino transport methods (see, e.g., Just et al. 2015; O'Connor 2015; Kuroda et al. 2016; Pan et al. 2019; Glas et al. 2019b). However, broad studies of multidimensional, long-time simulations up to 10 s after bounce are yet not feasible with state-of-the-art transport methods, without sacrificing resolution. A consequence of the more approximate leakage scheme is an incorrect electron fraction, typically leaning toward more neutron-rich values (Dessart et al. 2009; Pan et al. 2019). We discuss corrections to the electron fraction for nucleosynthesis calculations in Section 5.

We use the LS220 EOS of Lattimer & Swesty (1991) for the high-density regions. In the outer layers of the progenitor and at late times, the density reaches very low values ($\rho \lesssim 10$ g cm^{-3}); therefore, we use a hybrid EOS approach with a transition to the Helmholtz EOS (Timmes & Arnett 1999; Fryxell et al. 2000; Timmes & Swesty 2000) at around $5-1 \times 10^5$ g cm^{-3}.

2.2. Progenitor Models and Rotation

In this study, we use three different progenitors with zero-age main sequence mass 11.2, 15, and $27\,M_\odot$, namely the s11.2, s15.0, and s27.0 models from Woosley et al. (2002). All three progenitor models are nonrotating. As we aim to explore the effect of rotation on the explosion phase and on the long-time evolution, we superimpose a parametric rotational profile of the form

$$\Omega(r) = \Omega_0 \cdot \frac{1}{1 + (r/r_A)^2}. \qquad (1)$$

We set the characteristic radius r_A to a fixed value of 3000 km (approximately the extent of the Fe and Si core in the s15 progenitor; see Müller et al. 2004; Buras et al. 2006) and use Ω_0 as a free parameter to adjust the rotation strength. In addition to a nonrotating case ($\Omega_0 = 0$), we use six different rotation strengths: $\Omega_0 = (0.01,\ 0.03,\ 0.06,\ 0.10,\ 0.20,\ 0.30) \times (2\pi$ rad s^{-1}). The three first values correspond to moderately rotating models (compare to, e.g., Heger et al. 2005; Ott et al. 2006; Burrows et al. 2007) and the three last ones to rapidly rotating models.

We label our models with their corresponding progenitor, heating factor, and rotation strength. For example, the label s15_F130_R006 refers to a simulation of the s15.0 progenitor with $f_{heat} = 1.3$ and $\Omega_0 = 0.06 \times 2\pi$ rad s^{-1}.

2.3. Tracer Particles and Nucleosynthesis Network

In order to estimate the nucleosynthesis, we need the Lagrangian evolution of the matter ejected. Since the FLASH code is Eulerian, we use a tracer particle scheme to track individual fluid elements (also called tracer particles, trajectories, and mass elements). The tracers are not included in the simulation but calculated from the output (see, e.g., Harris et al. 2017 for a detailed discussion). All tracer particles have equal mass and are distributed proportional to the density (see Dubey et al. 2012 for tracers in the FLASH code). For the s15.0 progenitor, we initialize 21,281 particles at the beginning of the simulation. This corresponds to a mass of $1.76 \times 10^{-4}\,M_\odot$ per tracer that is similar to the "medium resolution" case in Nishimura et al. (2015). The amount of matter ejected by the tracers agrees within 1% with the unbound material obtained directly from the hydrodynamics.

In addition to the evolution of density and temperature along the tracers, we also need the electron fraction. However, this is poorly determined in our simulations because we use a gray neutrino leakage scheme. Therefore, we correct the electron fraction to estimate the nucleosynthesis within some uncertainties (see Section 5 for more details).

For the nucleosynthesis calculations, we use the nuclear reaction network code WinNet (Winteler 2011; Winteler et al. 2012). The reaction rates include the JINA Reaclib compilation (Cyburt et al. 2010), theoretical weak reactions from Langanke & Martínez-Pinedo (2001), and neutrino reactions from Langanke & Kolbe (2001, see also Fröhlich et al. 2006 for details about the neutrino reactions). For all nucleosynthesis calculations, we evolve the electron fraction in nuclear statistical equilibrium (NSE) at a temperature of 20 GK and assume NSE down to 6.5 GK.

Table 1
Overview of Models

Name	Prog.	$f_{\rm heat}$	Ω_0 (2π rad s^{-1})	$t_{\rm end}$ (s)	$t_{\rm exp}$[a] (s)	$d_{\rm shock}$[b]	$E_{\rm exp}^{100\rm msc}$ (B)	$E_{\rm exp}^{\rm final}$ (B)	$M_{\rm ej}$[d] ($M_\odot$)	$M_{\rm PNS}$ ($M_\odot$)	$t_{\rm wind}$[e] (s)
s15_F100_R000	s15.0	1.00	0.00	1.55	⋯	⋯	⋯	⋯	⋯	1.98	⋯
s15_F105_R000	s15.0	1.05	0.00	1.54	⋯	⋯	⋯	⋯	⋯	1.98	⋯
s15_F105_R003	s15.0	1.05	0.03	1.55	⋯	⋯	⋯	⋯	⋯	1.98	⋯
s15_F105_R020	s15.0	1.05	0.20	1.45	⋯	⋯	⋯	⋯	⋯	1.96	⋯
s15_F108_R000	s15.0	1.08	0.00	8.96	1.07	1.26	0.04	1.16	0.76	2.16	0.00
s15_F110_R000	s15.0	1.10	0.00	8.14	0.93	1.06	0.04	1.41	0.90	2.10	0.00
s15_F110_R001	s15.0	1.10	0.01	1.63	⋯	⋯	⋯	⋯	⋯	1.99	⋯
s15_F110_R003	s15.0	1.10	0.03	1.54	⋯	⋯	⋯	⋯	⋯	1.98	⋯
s15_F110_R020	s15.0	1.10	0.20	1.46	⋯	⋯	⋯	⋯	⋯	1.96	⋯
s15_F115_R000	s15.0	1.15	0.00	9.25	0.92	1.01	0.04	1.34	0.93	2.20	0.00
s15_F115_R003	s15.0	1.15	0.03	1.61	⋯	⋯	⋯	⋯	⋯	1.99	⋯
s15_F120_R000	s15.0	1.20	0.00	7.89	0.28	0.94	0.14	1.21	0.86	2.03	0.00
s15_F120_R001	s15.0	1.20	0.01	6.74	0.30	0.87	0.19	1.20	0.76	1.95	0.00
s15_F120_R003	s15.0	1.20	0.03	9.31	0.36	0.29	0.15	0.70	1.28	1.80	2.44
s15_F120_R006	s15.0	1.20	0.06	6.03	0.38	0.77	0.11	0.63	0.88	1.86	0.00
s15_F120_R010	s15.0	1.20	0.10	1.61	⋯	⋯	⋯	⋯	⋯	1.99	⋯
s15_F120_R020	s15.0	1.20	0.20	1.46	⋯	⋯	⋯	⋯	⋯	1.96	⋯
s15_F130_R000	s15.0	1.30	0.00	9.26	0.23	0.59	0.15	0.79	1.42	1.75	1.73
s15_F130_R001	s15.0	1.30	0.01	4.60	0.22	0.37	0.27	1.00	0.82	1.85	0.00
s15_F130_R003	s15.0	1.30	0.03	8.63	0.23	0.37	0.22	0.75	1.52	1.68	3.48
s15_F130_R006	s15.0	1.30	0.06	4.17	0.24	0.25	0.28	0.73	0.59	1.87	0.00
s15_F130_R010	s15.0	1.30	0.10	9.08	0.28	−0.00	0.24	0.64	1.40	1.72	5.10
s15_F130_R020	s15.0	1.30	0.20	9.25	0.32	−0.13	0.19	0.77	1.34	1.75	2.46
s15_F130_R030	s15.0	1.30	0.30	9.30	0.36	0.20	0.15	0.67	1.26	1.76	3.60
s15_F150_R000	s15.0	1.50	0.00	7.96	0.17	0.64	0.30	1.21	1.13	1.87	0.00
s15_F150_R001	s15.0	1.50	0.01	7.69	0.17	0.68	0.36	1.12	1.31	1.71	0.16
s15_F150_R003	s15.0	1.50	0.03	9.43	0.21	0.24	0.40	1.09	1.59	1.69	3.37
s15_F150_R006	s15.0	1.50	0.06	9.03	0.17	0.19	0.36	0.91	1.56	1.69	5.34
s15_F150_R010	s15.0	1.50	0.10	8.00	0.21	0.22	0.31	0.73	1.55	1.69	4.81
s15_F150_R020	s15.0	1.50	0.20	8.94	0.22	−0.21	0.37	0.83	1.57	1.67	4.81
s15_F150_R030	s15.0	1.50	0.30	9.40	0.21	0.18	0.16	0.81	1.42	1.69	3.80
s11_F100_R000	s11.2	1.00	0.00	4.36	0.16	0.36	0.04	0.36	0.41	1.33	0.00
s11_F100_R003	s11.2	1.00	0.03	4.43	0.25	0.19	0.04	0.44	0.33	1.39	0.00
s11_F100_R020	s11.2	1.00	0.20	4.63	0.25	0.61	0.02	0.64	0.31	1.40	0.00
s27_F105_R000	s27.0	1.05	0.00	3.79	1.42	0.93	0.05	0.67	0.27	2.22	0.00
s27_F105_R003	s27.0	1.05	0.03	1.82	⋯	⋯	⋯	⋯	⋯	2.07	⋯
s27_F105_R020	s27.0	1.05	0.20	1.73	⋯	⋯	⋯	⋯	⋯	2.05	⋯
s27_F110_R000	s27.0	1.10	0.00	3.06	0.31	0.63	0.07	0.33	0.17	1.93	0.00
s27_F110_R003	s27.0	1.10	0.03	1.30	0.54	0.39	0.05	0.23	0.09	1.87	0.00
s27_F110_R020	s27.0	1.10	0.20	2.06	⋯	⋯	⋯	⋯	⋯	2.12	⋯
s27_F120_R000	s27.0	1.20	0.00	2.89	0.29	0.72	0.07	0.65	0.39	2.02	0.00
s27_F120_R003	s27.0	1.20	0.03	1.79	0.34	0.59	0.10	0.55	0.19	1.91	0.00
s27_F120_R020	s27.0	1.20	0.20	2.11	⋯	⋯	⋯	⋯	⋯	2.13	⋯
s27_F130_R000	s27.0	1.30	0.00	3.47	0.21	0.73	0.07	1.24	0.55	2.09	0.00
s27_F130_R003	s27.0	1.30	0.03	2.85	0.20	0.55	0.10	0.90	0.38	2.00	0.00
s27_F130_R020	s27.0	1.30	0.20	3.82	0.29	0.16	0.07	0.46	0.23	1.92	0.00

Notes.
[a] Post-bounce time when the maximum shock radius exceeds 600 km.
[b] Explosion energy at $t_{\rm exp}$ + 100 ms.
[c] Shock deformation parameter (Equation (2)) at $t_{\rm exp}$.
[d] Mass of ejected (unbound) matter at the end of the simulation.
[e] Total duration of neutrino-driven wind phases ($\dot{M}_{\rm acc,500\ km} = 0$).

3. Overview of Models and Explosions

We present here all our models including 32 explosion models (see Table 1 for an overview). We also include unsuccessful explosions in the table for completeness. These models were continued for 1–2 s after bounce but did not show signs of shock revival until then. First, we focus shortly on the explosion phase and discuss the long-time evolution in more detail later (Section 4). We are aware that our results are only qualitative because the neutrino transport is approximated and we artificially increase the energy deposited by neutrinos to trigger explosions.
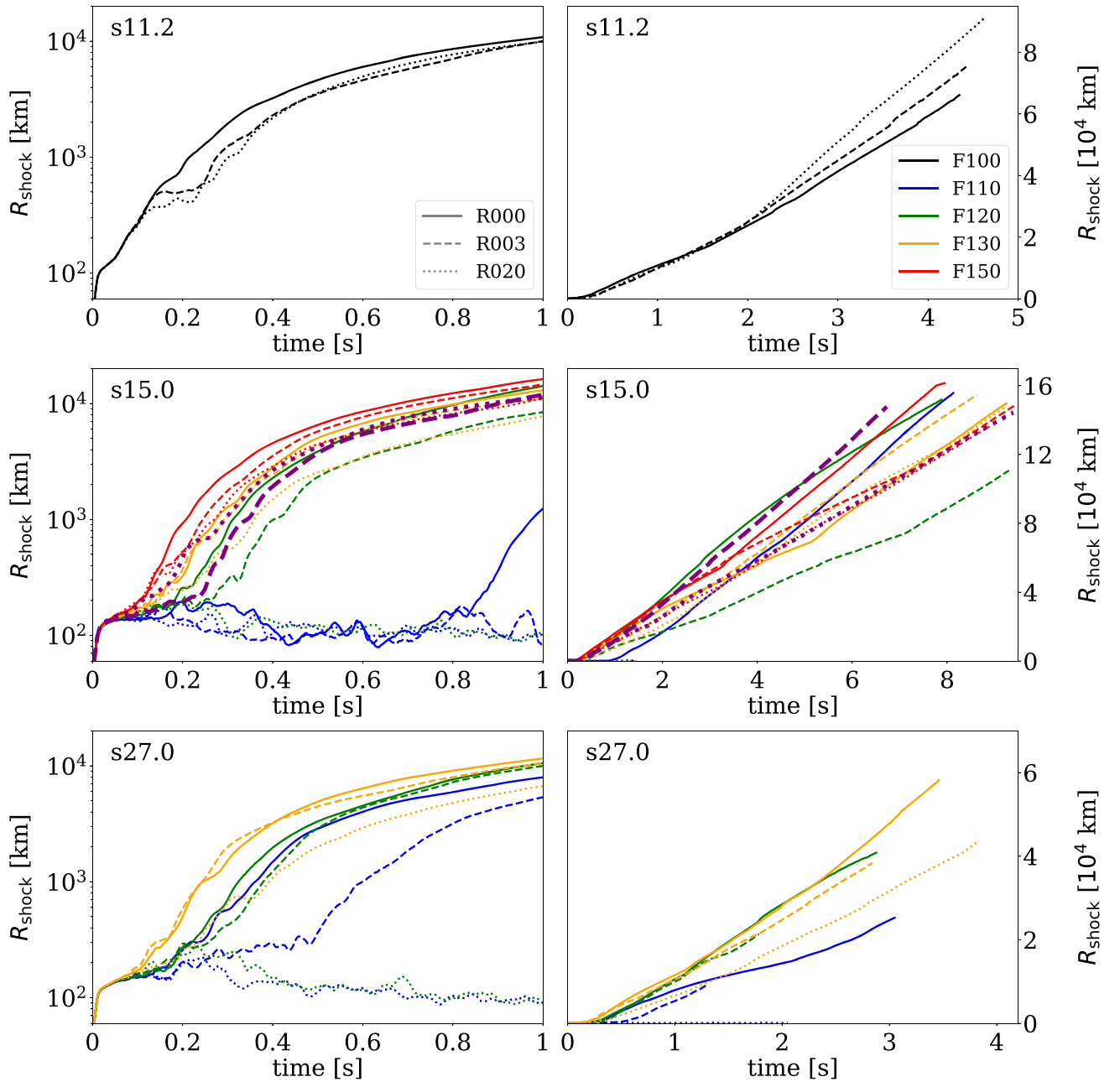
Figure 1. Early (left column) and long-time (right column) evolution of the maximum shock radii for the three progenitors (s11.2, s15.0, and s27.0 in the top, middle, and bottom panels, respectively). Different rotation rates are indicated by different line styles and various heating factors by colors, as given in the figures. The dashed and dotted purple lines represent the models s15_F120_R001 and s15_F150_R030, respectively.

Recent work of Nagakura et al. (2021) shows the impact of accretion on the neutrino emission based on long-time, 2D simulations with accurate neutrino transport. Moreover, our simulations are 2D and this favors some artificial features and may amplify some of our conclusions, like the persistence of downflows. However, we are able to explore the long-time evolution for a big sample of models and we find trends and correlations that are robust and are present also in 3D simulations with better neutrino treatment (e.g., see Müller 2015; Janka et al. 2016; Summa et al. 2018; Burrows et al. 2019; Müller et al. 2019; Vartanyan et al. 2019b; Bollig et al. 2021; Iwakami et al. 2020; Stockinger et al. 2020).

The evolution of the shock radius is shown in Figure 1 for the three progenitors and for three rotation rates. The lightest

progenitor, s11.2, explodes without additional neutrino heating within 0.25 s for all variations of the rotation. Therefore, we only use $f_{\rm heat} = 1$ for this progenitor. For the heavier progenitors, the threshold for shock revival in nonrotating models is $f_{\rm heat} = 1.08$ and 1.05 for s15.0 and s27.0, respectively. This is in agreement with estimates from progenitor compactness (O'Connor & Ott 2011), which has values of $\xi_{1.75} = 0.07$, 0.54, and 0.53 for the s11.2, s15.0, and s27.0 models, respectively (Pan et al. 2016; Summa et al. 2016). The explosion time varies depending on the progenitor and the heating factor and it is also affected by rotation.

In the presence of rotation, we notice that shock revival generally occurs later, or fails overall (see also, e.g., Fryer & Heger 2000; Thompson et al. 2004; Summa et al. 2018; Obergaulinger & Aloy 2020). This can be understood from a reduction of mass

accretion through the stalled shock because of centrifugal forces. This leads to a diminished accretion luminosity and ultimately takes away support for the stalled shock. Moreover, rotation contributes to shift matter from the poles toward the equatorial plane and this has an impact on the neutrino luminosities in different directions.

Anisotropic emission of neutrinos in rotating CCSN has already been reported in early multidimensional simulations (Fryer & Heger 2000; Buras et al. 2003; Kotake et al. 2003; Thompson et al. 2004; Marek & Janka 2009). The described behavior may be artificially enhanced in two-dimensional simulations, although, modern simulations in three dimensions also predict smaller luminosities in rapidly rotating cases (Summa et al. 2018; Obergaulinger & Aloy 2020). However, nonaxisymmetric spiral modes can increase the mass in the gain region leading to a fundamentally different explosion behavior in 3D (Nakamura et al. 2014; Summa et al. 2018; Kuroda et al. 2020).

4. Long-time Evolution

The 32 exploding models are evolved for several seconds (see Table 1) and we define the "long-time" phase starting one second after the explosion, i.e., $t > t_{exp} + 1$ s. The long-time evolution is characterized by a continuous increase of the explosion energy due to long-lasting accretion onto the PNS. This accretion depends on the formation and evolution of downflows and it is correlated with rotation and to the morphology of the early explosion phase. In the following, we discuss the generation of explosion energy (Section 4.1), how this is affected by rotation and by the explosion morphology (Section 4.2), and the evolution of key quantities during the long-time evolution phase (Section 4.3).

4.1. Explosion Energy Generation

The explosion energy (E_{exp}) is calculated by adding the energy of all unbound matter[9] and it is shown in Figure 2 for the three progenitors including different heating factors and rotation rates. We note that our definition corresponds to the "diagnostic" explosion energy, in the sense that it is not the final, saturated value. Shortly after the explosion, E_{exp} rapidly grows and in some cases it looks like it saturates and stays constant. However, for all models the explosion energy continues slowly increasing over seconds due to the long-lasting accretion (see also Bruenn et al. 2013; Nakamura et al. 2015; Bruenn et al. 2016; Nakamura et al. 2016; Summa et al. 2016; Harris et al. 2017; Müller et al. 2017; O'Connor & Couch 2018; Summa et al. 2018; Vartanyan et al. 2018; Müller et al. 2019; Glas et al. 2019b; Vartanyan et al. 2019b; Bollig et al. 2021; Stockinger et al. 2020; Nagakura et al. 2021). This is in contrast to one-dimensional models that by definition cannot account for downflows and the explosion energy saturates promptly and stays constant (e.g., see Arcones et al. 2007; Perego et al. 2015; Couch et al. 2020). Even if long-lasting downflows in 2D simulations may become stable and artificially stay for too long, there are also 3D simulations showing downflows and accretion at late times (Burrows et al. 2019; Vartanyan et al. 2019b; Bollig et al. 2021; Stockinger et al. 2020).

With our large set of models, we can investigate the impact of different key aspects on the explosion energy.

Downflows are a multidimensional, long-time, and angular-dependent features that are correlated to the explosion energy growth (see also Nagakura et al. 2021 for the long-time impact of accretion on the neutrino emission). We investigate the angular dependency of the downflows and explosion energy evolution defining the explosion energy growth rate as $\dot{E}_{exp} \equiv dE_{exp}/dt$ and comparing to the mass accretion at late times. Downflows are derived from the mass accretion rate ($\dot{M}_{acc}$) through a sphere with a 500 km radius around the PNS. For model s15_F120_R001, Figure 3 shows the direction of downflows over time (upper panel) and how it is correlated to the explosion energy generation (bottom panel). Before the explosion ($t \lesssim 0.3$ s post bounce), there is only accretion. The explosion energy is first accumulated isotropically at shock revival. During the first seconds, the shock expands prominently toward the southern hemisphere leaving space for a long-lasting downflow from the northern hemisphere. Initially, the explosion energy grows also in the directions of downflows, because we measure the accretion only at a 500 km radius, but explosion energy is also accumulated below that radius. When the downflow is firmly established after $t \approx 1$ s, explosion energy is generated almost exclusively in the southern hemisphere. The accreted matter acts as fuel for the supernova energy. The strong downflow from the northern hemisphere gradually changes its direction during $2 < t < 4$ s to the southern hemisphere and the explosion energy generation rate shifts its direction accordingly. The gravitational pull of the PNS decreases the velocity of some ejecta and leads to initially unbound matter to be bound again, which can be seen in slightly negative values of $\dot{E}_{exp}$ in the southern hemisphere. Until the end of the simulation at $t = 6.74$ s, the downflow changes direction again and there are no signs of vanishing mass accretion yet.

In some cases, we obtain explosions with less stable downflows where even an NDW can form, as shown in Figure 4 for the model s15_F150_R030. The NDW phase ($3.5 < t < 6.5$ s) is characterized by a vanishing mass accretion rate, $\dot{M}_{acc} = 0$, and matter is ejected in all directions (subsequently, we define NDW phases by having $\dot{M}_{acc} = 0$ for at least a 10 ms duration). During this wind phase, considerably less explosion energy is added. However, $\dot{E}_{exp}$ does not vanish completely, since there is a continuous outflow of matter ejected by neutrinos when depositing energy in the layers around the PNS. At $t \approx 6.5$ s, the wind is terminated by a downflow, and consequently a new phase of explosion energy generation sets in. This transition occurs almost instantaneously. For all models that develop a wind (see Section 4.3), we see typical integrated values of $\dot{E}_{exp} \approx 0.04$ B s^{-1} during phases of no accretion. Our results suggest that this ongoing interplay of accretion and ejection can continue for longer than previously thought. However, 3D simulations would be necessary to conclude the impact and duration of downflows and NDWs.

4.2. Impact of Rotation and Explosion Morphology

The generation of explosion energy through mass accretion at late times is a robust mechanism in our models. At one second after the explosion (i.e., at the start of the long-time phase), the initial shock wave has reached a radius of $(1-2) \times 10^4$ km, has cooled down to $T \sim 0.5$–1.5 GK, and has reached densities of

---

[9] In the calculation of the explosion energy we do not consider the contribution of the outer layers (see, e.g., Bruenn et al. 2013, 2016). We estimate that this "overburden" contribution will be around $E_{ov} \ll 0.1$ B in our models, which is not important for our overall qualitative description.
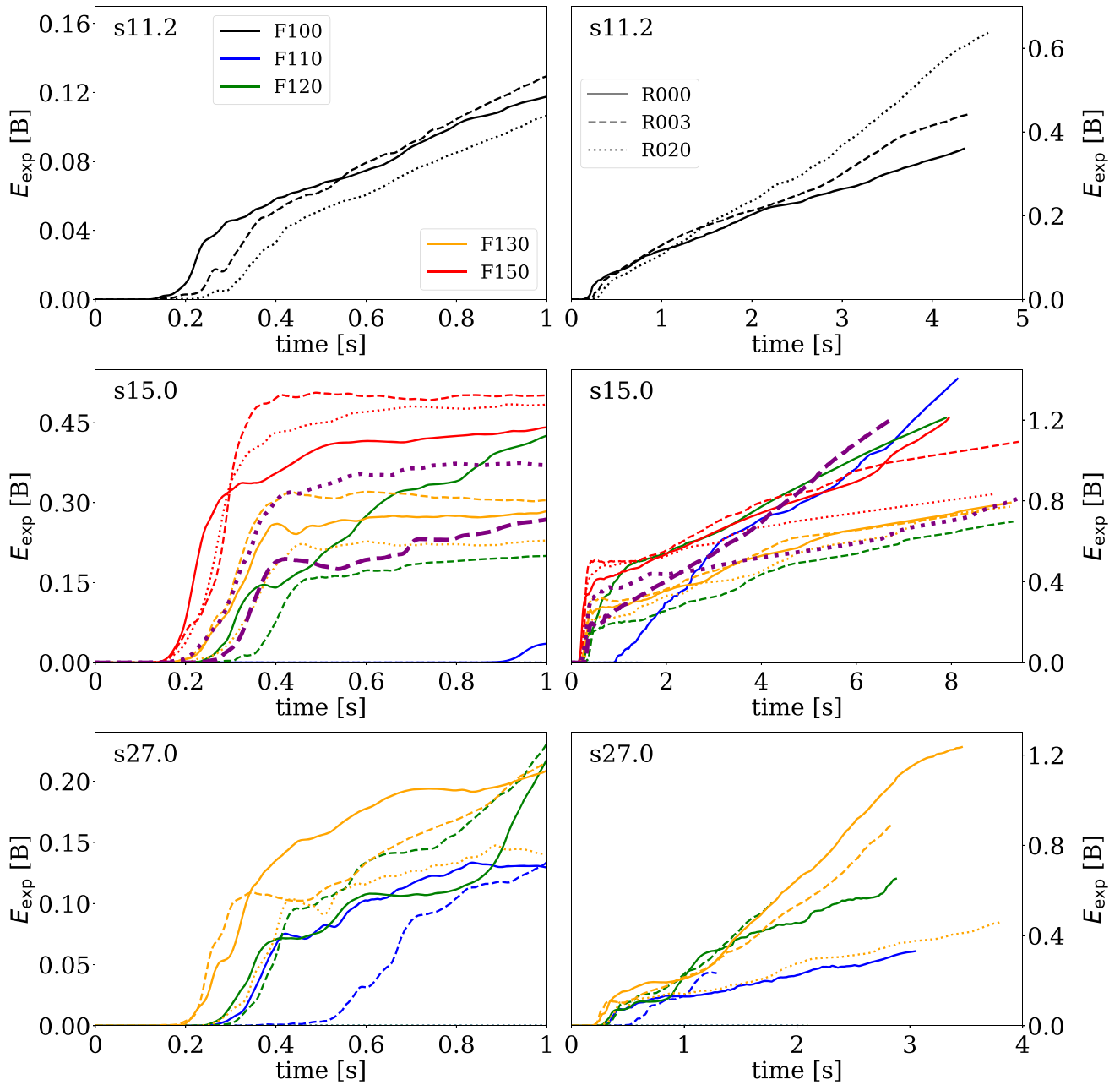
Figure 2. Same as in Figure 1, but for the explosion energy. The dashed and dotted purple lines represent the models s15_F120_R001 and s15_F150_R030, respectively.

$\rho \sim 10^5 \, \mathrm{g \, cm^{-3}}$. At this point, the explosion energy stored within the shock wave and the ejecta generated earlier is approximately constant and any additional E_exp generation originates from the vicinity of the PNS. Therefore, there is a correlation between $\dot{M}_\mathrm{acc}$ and $\dot{E}_\mathrm{exp}$ for all exploding models, as shown in Figure 5. In this figure both quantities are shown for the long-time evolution, i.e., $t > t_\mathrm{exp} + 1 \, \mathrm{s}$. The gray dots correspond to individual times (each dot is a mean value over a 5 ms time interval) of all simulations and the colored symbols are obtained by averaging during the whole long-time phase. This introduces some bias for models with short simulation times because the mass accretion is higher during the first seconds. In any case, there is a correlation of late-time accretion and explosion energy growth rate. In NDW phases of no accretion, the explosion energy growth rate adopts

values of $\dot{E}_\mathrm{exp,NDW} = (0.035 \pm 0.007) \, \mathrm{B \, s^{-1}}$ (left panel of Figure 5). We note that this specific value might be influenced by our use of a gray neutrino leakage scheme and Newtonian gravity.

The early shock morphology has a clear impact on the formation of stable downflows and thus on the late evolution of accretion. In order to quantify the shock morphology, we employ the shock deformation parameter introduced by Scheck et al. (2006). It uses the shock radius R_s as a function of the polar angle θ and is given by

$$d_\mathrm{shock} = \frac{\max[R_\mathrm{s}(\theta)\cos(\theta)] - \min[R_\mathrm{s}(\theta)\cos(\theta)]}{2 \cdot \max[R_\mathrm{s}(\theta)\sin(\theta)]} - 1. \quad (2)$$

The parameter is equivalent to the ratio of the maximum shock diameters, parallel and perpendicular to the cylindrical axis. It
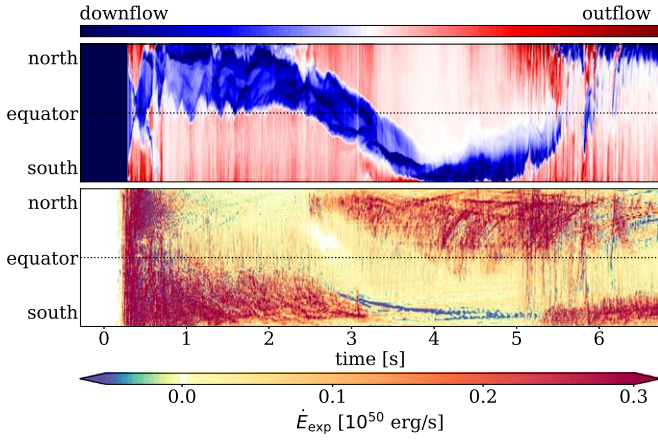
Figure 3. Directionality of downflows and explosion energy generation in model s15_F120_R001. The upper panel shows mass downflows and outflows (relative strength, at $r = 500$ km) in a $t-\theta$ plane, i.e., direction dependent, with the equator being perpendicular to the cylindrical axis. The lower panel shows the explosion energy generation rate in the same plane. The direction in which explosion energy is generated depends on the direction of downflows. Time $t = 0$ s corresponds to bounce.
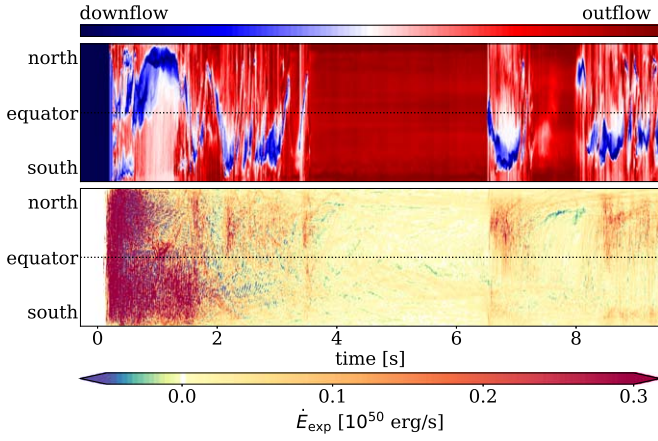

Figure 4. Same as in Figure 3, but for model s15_F150_R030, which has a phase of no accretion corresponding to a neutrino-driven wind (NDW).
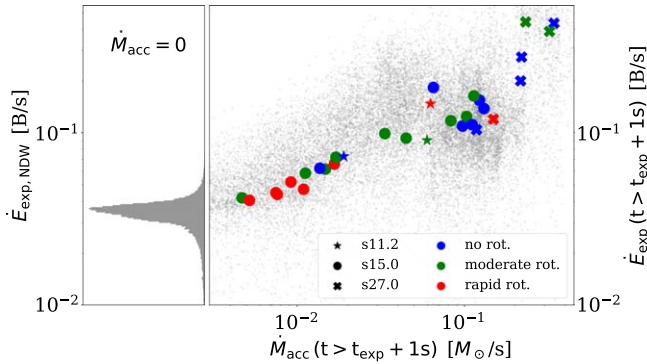
Figure 5. Right panel: growth rate of the explosion energy vs. mass accretion at late times (i.e., $t > t_{exp} + 1$ s). The gray dots represent individual data points (shown as running averages of 5 ms length) from all simulations during the long-time evolution, while the colored symbols indicate the mean values from different models for that phase. Left panel: density distribution of $\dot{E}_{exp}$ during NDW phases with $\dot{M}_{acc} = 0$.

can have positive and negative values, for a prolate and an oblate shock deformation, respectively. In the case of a spherical shock expansion, d_{shock} becomes zero. We find a
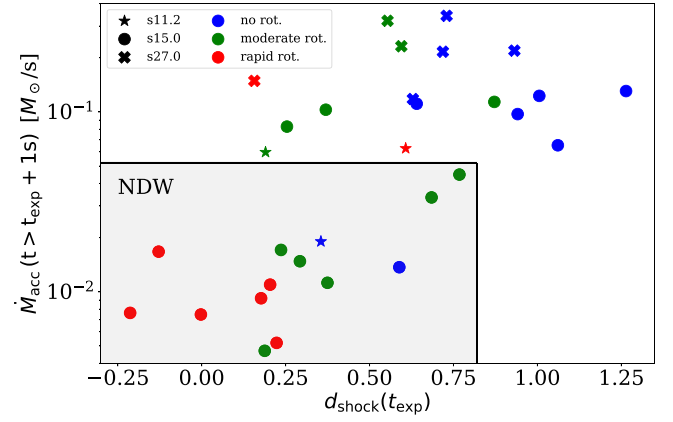
Figure 6. Average late-time accretion rate vs. the shock deformation parameter at explosion time for the three progenitors (different symbols) and various rotation strengths (different colors). Models within the shaded area have a phase of zero accretion in all directions or an NDW during the long-time evolution.

correlation between the shock deformation parameter at the time of shock revival and the rotation strength (see Table 1). Nonrotating 2D simulations typically explode in a prolate morphology, which is a known feature of this geometry (see, e.g., Müller 2015; Nakamura et al. 2015; Bruenn et al. 2016; Summa et al. 2016; O'Connor & Couch 2018; Vartanyan et al. 2018). However, the resulting accretion along preferred directions has also been observed in 3D simulations (Burrows et al. 2019; Vartanyan et al. 2019b).

Rapidly rotating models tend to have less accretion due to the increased centrifugal forces, which reduce the infall velocity of matter from the equatorial plane and therefore also the accretion rate. The impact of rotation is present in all phases of a CCSN. With increased rotation rate, the shock morphology becomes more spherical and eventually also slightly oblate for rapidly rotating models. Exceptions here are simulations of the s11.2 progenitor, due to the smaller amount of angular momentum (a factor of 10 less than for s15.0 models with the same rotation rate) and an earlier explosion time, which allows for less angular momentum to be accreted before shock revival.

We can investigate the relation between shock deformation (Equation (2)) and late mass accretion. Downflows usually originate from directions with moderate early shock expansion. In those directions, part of the ejected matter does not reach the escape velocity and eventually falls back onto the PNS. Figure 6 shows the relation of the early shock morphology $d_{shock}(t_{exp})$ and the mass accretion at late times. There is not a clear correlation of these two quantities but some trends. Simulations exploding with $d_{shock}(t_{exp}) \geqslant 0.5$ are typically moderately rotating or nonrotating (with the exception of the model s11_F100_R020) and consistently have an average mass accretion at late times of $\dot{M}_{acc} > 0.01 \, M_{\odot} \, \text{s}^{-1}$. Furthermore, we can separate all simulations in two groups depending on whether they have some phase of zero accretion. The models that develop an isotropic NDW are in the lower left corner region corresponding to lower late accretion and not extreme shock deformation. Notice that there may be short-duration winds simultaneously with accretion in another direction and those are not discussed here.
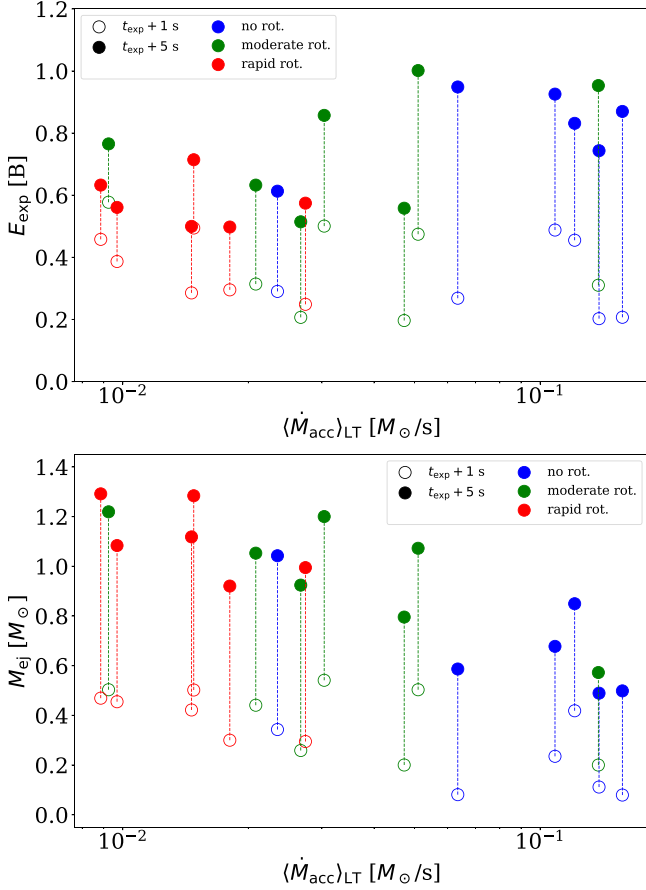
Figure 8. Time lines of s15.0 progenitor simulations, where red areas mark the presence of an isotropic NDW phase. We omit the "s15_" prefix in the model names.

Figure 7. Influence of the long-time evolution on the explosion energy (upper panel) and mass ejection (bottom panel) related to the mass accretion. Colors indicate the rotation strength. Open and filled circles show the explosion energy at 1 s and 5 s after shock revival, respectively. The mass accretion is averaged for the time interval $1 < t - t_{exp} < 5$ s denoted as LT for long-time.

4.3. Evolution in the Long-time Phase and the Neutrino-driven Wind

As shown in previous section, there is a strong link between the shock deformation and the formation of stable downflows that critically affect the explosion energy. Here, we want to study the long-time evolution of the explosion energy and mass ejection. For the s15 progenitor, we compare these quantities at two different times, 1 and 5 s after shock revival.

The evolution of the explosion energy and its dependence on the mass accretion is shown in Figure 7, upper panel. At 1 s after shock revival, the explosion energy of all models is distributed at (0.4 ± 0.2) B, independent of the rotation strength and mass accretion. During the next 4 s, rapidly rotating models increase their explosion energy by ~ 0.4 B and end up with values below 0.8 B at $t_{exp} + 5$ s. By contrast, moderately rotating and nonrotating models gain considerably more energy during this same time, reaching around 0.9–1 B. The value for nonrotating models is also in good agreement with recent 3D studies (Bollig et al. 2021). We note that for simulations that run for a longer time, the final explosion energy keeps increasing after $t_{exp} + 5$ s and the trend with rotation is consistent also at later times. Therefore, we conclude that, for models with initial morphology favorable for large-scale downflows, the saturation point of the explosion energy lies beyond 10 s after the initial explosion.
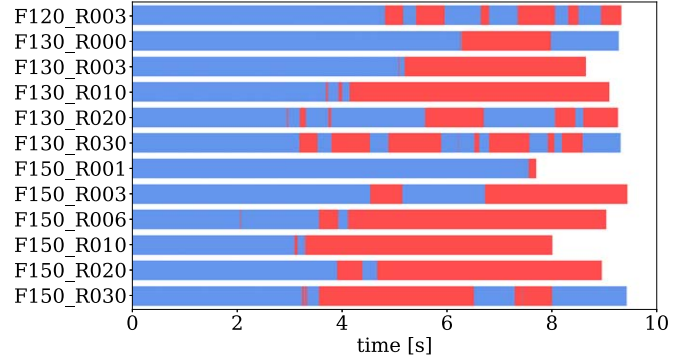
The long-time evolution is also critical for nucleosynthesis (Section 5); therefore, here we investigate the amount of mass ejected (Figure 7, bottom panel). At 1 s after shock revival, models with lower accretion (corresponding to approximately spherical explosions; Figure 6) have ejected more mass than those with strong downflows and a prolate morphology. This is due to the more energetic shock expansion into the equatorial direction in spherical models compared to prolate explosions. This trend continues also in the next seconds. We calculate the average energy of ejected matter: for low accretion models (spherical explosions), we obtain values of $E_{exp}/M_{ej} \approx 0.5$ B $M_\odot^{-1}$, while models with high accretion and prolate morphologies reach $E_{exp}/M_{ej} \approx 1.5$ B $M_\odot^{-1}$ at 5 s.

Even if a considerable amount of mass is ejected in all exploding models, a wind develops only in 12 of the 21 exploding models for the s15 progenitor. These isotropic NDW phases ($\dot{M}_{acc} = 0$ for at least 10 ms duration) are shown in red in Figure 8. The first wind phases start to appear after $t \approx 3$ s. There are two kinds of NDW phases: short and long duration. The termination of this phase is usually due to large accumulations of matter with a negative radial velocity above the wind. We show examples of the two possible NDW phases in Figure 9. Here, the symmetry axis is displayed horizontally and we show the density in the upper half of the domain, and the radial velocity in its lower half. The NDW regions are visible around the high-density region with the PNS in the center, and are characterized by high, supersonic velocities, a steep density gradient, and the wind termination shock, where the density (velocity) increases (decreases) abruptly. In the example of model s15_F150_R030, one can see the matter accumulations with a negative radial velocity and comparably high density just above the wind termination shock. Long-duration winds can extend up to a several 10^4 km radius (see model s15_F150_R020 in Figure 9). The duration of the wind depends on the heating factor and rotation rate. When increasing the heating factor and/or the rotation, there is lower mass accretion and this allows a wind to form and last for several seconds. Other 2D and 3D simulations indicate also that there is not always a wind after a successful explosion (see, e.g., Bruenn et al. 2016; O'Connor & Couch 2018; Vartanyan et al. 2019b; Bollig et al. 2021).

5. Nucleosynthesis

Since our neutrino treatment is very simple, the following nucleosynthesis results are only approximate, even if we correct the neutrino properties affecting the evolution of the electron fraction. We focus only on the 21 exploding simulations of the
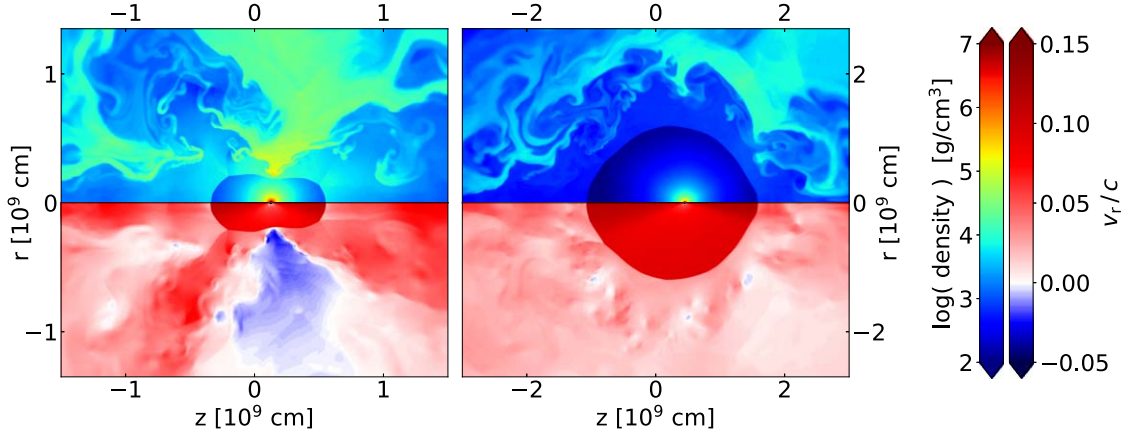
Figure 9. Density (top) and radial velocity (bottom) of model s15_F150_R030 (left) at 6.3 s shortly before termination of the wind (compare to Figure 4 and 8), and model s15_F150_R020 (right) at 8 s after bounce. Note the different axes scales for both models.

$15\,M_\odot$ progenitor (see Table 1). The amount of ejected mass (Figure 7) corresponds to several thousands of ejected tracers per model. These ejected tracers can be divided into "neutrino-processed" and "shock-processed". Tracers are considered neutrino-processed when their electron fraction changes by $|\Delta Y_e| > 0.01$ compared to their starting value. Most of these tracers reach a rather high temperature and enter NSE resetting the progenitor composition. Shock-processed particles retain their original electron fraction; their temperature is high enough to change slightly the progenitor composition, but most of them stay too cold to enter NSE.

For the cold, shock-processed tracers that do not reach NSE, the evolution of Y_e is not affected by neutrinos. Therefore, for these tracers we use the electron fraction obtained in the simulations. By contrast, the hot tracers are sensitive to neutrino quantities that determine Y_e, namely neutrino and antineutrino energies and number luminosities (Qian & Woosley 1996). Therefore, for those tracers we try different corrections to cover all possible conditions. We investigate two different corrections to the Y_e based on one model and later extend our study to the remaining 20 explosions of the $15\,M_\odot$ progenitor. We select model s15_F120_R006 as reference here because it is the closest to the "s15" model in Wanajo et al. (2018) when comparing t_{exp}, E_{exp}, M_{PNS}, and $M_{ejected}$. However, our neutrino energies and luminosities based on the neutrino leakage scheme lead to unrealistically neutron-rich conditions.

In the determination of the electron fraction, there are two critical quantities: the energy difference between antineutrinos and neutrinos ($\Delta\epsilon_\nu = \langle\epsilon_{\bar{\nu}_e}\rangle - \langle\epsilon_{\nu_e}\rangle$) and the ratio of neutrino number luminosities ($RL_n = L_{n,\bar{\nu}_e}/L_{n,\nu_e}$). Following previous studies based on simulations with accurate neutrino transport (see, e.g., Liebendörfer et al. 2005; Bruenn et al. 2016; Takiwaki et al. 2016; Cabezón et al. 2018; Just et al. 2018; Kotake et al. 2018; O'Connor & Couch 2018; Summa et al. 2018; Vartanyan et al. 2018, 2019a; Müller 2019; Pan et al. 2019; Kuroda et al. 2020; Powell & Müller 2020), one can find typical energy differences of $\Delta\epsilon_\nu = \langle\epsilon_{\bar{\nu}_e}\rangle - \langle\epsilon_{\nu_e}\rangle \approx 2-2.5$ MeV. In our models we have on average $\Delta\epsilon_\nu = (2.3 \pm 0.6)$ MeV after the explosion time. Notice that anisotropic neutrino emission (Glas et al. 2019a; Nagakura et al. 2019b) can have also an impact on the Y_e distribution (Fujimoto & Nagakura 2019, 2021).

In our first approach, we use the original neutrino energies from our simulation and correct the luminosities similar to Sieverding et al. (2020), but adopting a constant luminosity
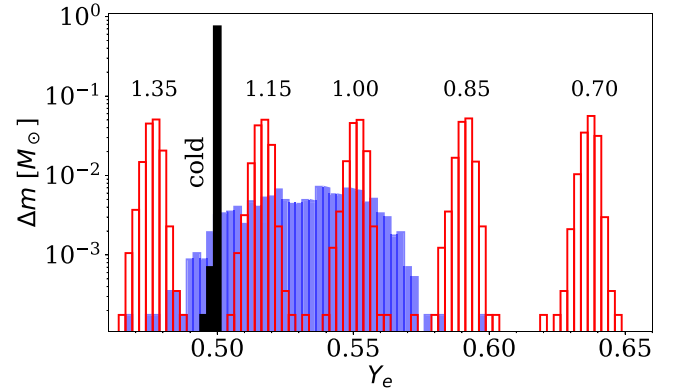

Figure 10. Modified distributions for the initial Y_e of model s15_F120_R006 when the trajectory cools down to 10 GK, or at their peak temperature for cold tracers. The black filled bars correspond to the cold (shock-processed) tracers for all distributions. The blue bars show the distribution with the original neutrino energies. The red bars show the distributions with fixed neutrino energy difference and fixed number luminosity ratios, which are indicated above.

ratio of $L_{n,\bar{\nu}_e}/L_{n,\nu_e} = 1.25$ instead of 1. This results in a Y_e distribution of ejected matter that is comparable to that in the studies of Wanajo et al. (2018) and Sieverding et al. (2020). The blue histogram in Figure 10 shows the corrected electron fraction distribution, with the cold tracers as black filled bars. The distributions for the hot tracers correspond to the initial electron fraction in the network calculations and corresponds to a temperature of $\sim$10 GK. For the hot tracers, the abundances obtained based on this distribution are shown in Figure 11 (left panel) where each line corresponds to an individual tracer and the colors indicate the Y_e value at 5.8 GK, i.e., around the temperature when the approximation of NSE breaks down.[10] Iron group nuclei dominate the final abundances and few tracers at the extremes of the Y_e distribution reach the region of Sr, Y, and Zr.

In our second approach to correct the Y_e, we change our neutrino energies to match more closely the literature values. We subtract 4 MeV from the $\bar{\nu}_e$ leakage energy and adopt a constant energy difference of $\Delta\epsilon_\nu = \langle\epsilon_{\bar{\nu}_e}\rangle - \langle\epsilon_{\nu_e}\rangle = 2$ MeV.

---

[10] Notice that between the initial Y_e at $\sim$10 GK shown in Figure 10 and the Y_e at 5.8 GK (Figure 11), the network assumes NSE, but the weak reactions are still evolved leading to an evolution of the electron fraction.
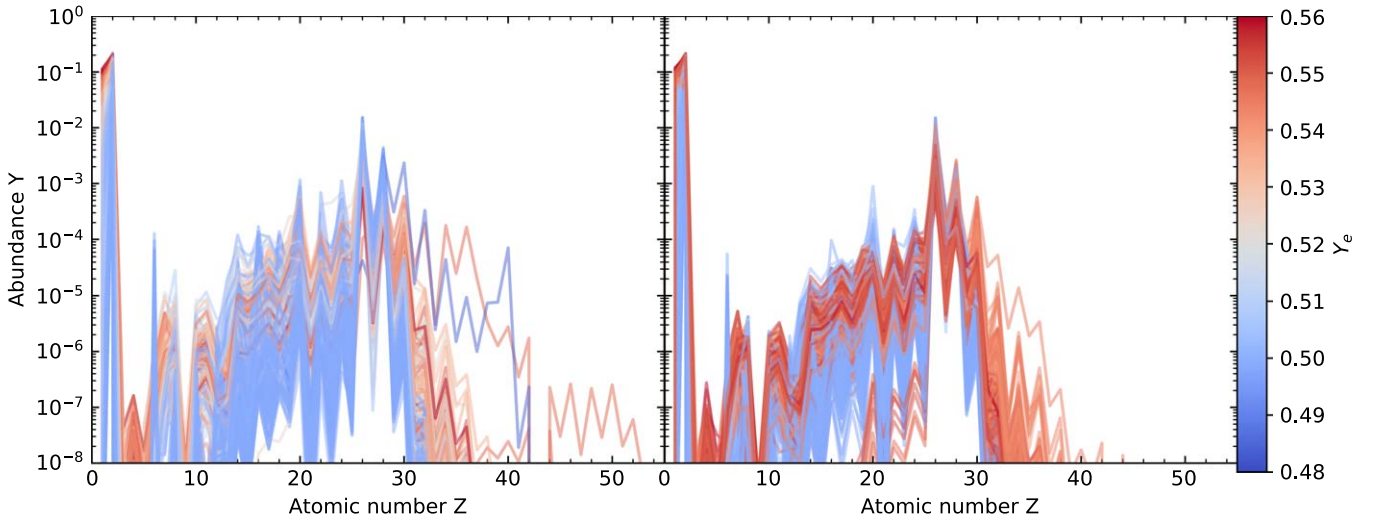
Figure 11. Abundances of all ejected neutrino-processed tracers of model s15_F120_R006 based on broad (left) and narrow with $RL_n = L_{n,\bar{\nu}_e}/L_{n,\nu_e} = 1$ (right) Y_e distributions shown in Figure 10. The colors of the lines indicate the electron fraction of the individual tracers at 5.8 GK.
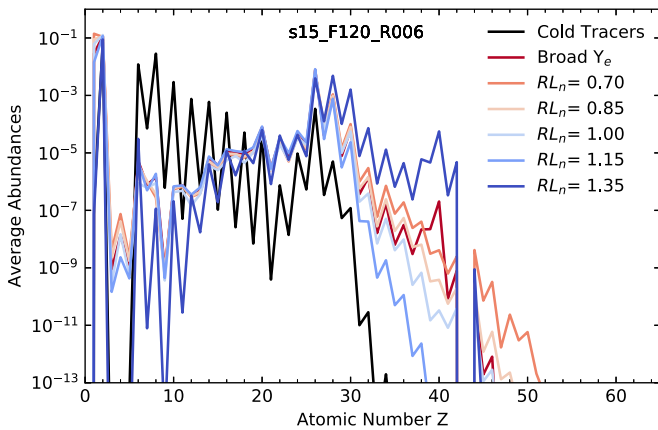

Figure 12. Integrated abundances of all trajectories of model s15_F120_R006 and different Y_e distributions as given in Figure 10.

Figure 13. Integrated abundances of all trajectories for all exploding models of s15 and the narrow Y_e distributions with $RL_n = 1$. The black lines represent the abundances from the shock-processed tracers from the different models.

Moreover, we parameterize the ratio of number luminosities, $RL_n = L_{n,\bar{\nu}_e}/L_{n,\nu_e} = 0.70, 0.85, 1.00, 1.15, 1.35$, where a smaller ratio corresponds to more proton-rich conditions. This correction leads to very narrow Y_e distributions as shown in Figure 10. These distributions disagree with those from state-of-the-art simulations, however they are very useful to understand how the abundances depend on a given electron fraction in the supernova ejecta and to cover all possible conditions. Figure 11 (right panel) shows the abundances for the hot tracers of model s15_F120_R006 based on the narrow distribution with $RL_n = L_{n,\bar{\nu}_e}/L_{n,\nu_e} = 1$. In that case as well, the majority of the produced nuclei lie in the iron peak, with a small portion of tracers producing nuclei with $Z > 30$.

The abundances for cold and hot tracers with different Y_e treatments are shown in Figure 12 for model s15_F120_R006. In general, the abundances for cold and hot tracers show a clear iron peak. The cold component is characterized by the odd–even distribution from carbon to calcium, following the progenitor composition. The hot component reaches heavier elements than the cold one with a slight dependency of the abundances on the exact electron fraction. The different assumptions for the initial Y_e lead to some variability for the abundances beyond iron covering all expected possibilities for
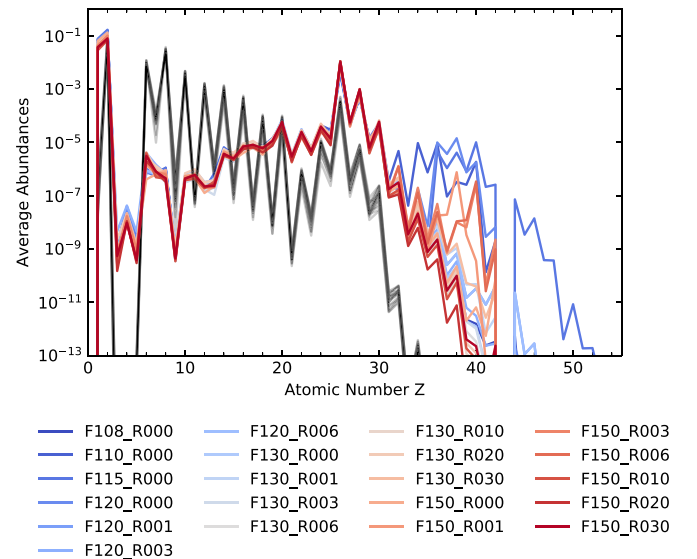
yields from neutrino-driven supernovae. The production of elements in the region of Sr, Y, and Zr is more efficient for slightly neutron-rich conditions, corresponding to $RL_n = 1.35$ (Arcones & Montes 2011; Arcones & Bliss 2014). We observe a very similar behavior and dependency of abundances on the Y_e distribution for all exploding models of the 15 $M_\odot$ progenitor. As a summary, we show in Figure 13 the final abundances only for the narrow Y_e distribution with $RL_n = 1$ for all models. We do not find any clear correlation between the abundances and the final explosion energy, although we see slight dependency on the explosion energy at ~1 s after bounce. The lack of correlation is probably due to our simple treatment of the neutrinos and the correction of the electron fraction, as well as to the fact that we are calculating abundances only for the 15 $M_\odot$ progenitor. Simulations with detailed neutrino transport and for several progenitors are necessary to narrow the uncertainties in the abundances and to
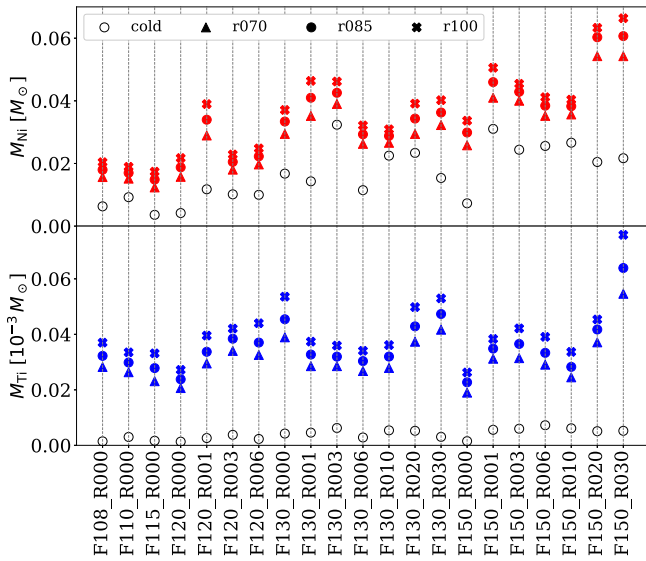
Figure 14. Yields of ^{56}Ni and ^{44}Ti obtained by post-processing the 21 exploding models. For each model, the yields are shown for the cold tracers (empty circles) and the neutrino-processed, hot tracers (filled symbols) for three different Y_e narrow distributions corresponding to $RL_n = 0.7$, 0.85, and 1 (triangles, circles, and crosses, respectively).

link those to other astrophysical conditions. Even if our results are not completely conclusive for abundances beyond iron, they indicate that there is not a strong variability for iron group elements. This may be important to estimate uncertainties in the production of ^{56}Ni and ^{44}Ti as shown in Figure 14 where we present an overview of all models including cold and hot components and variations of Y_e.

6. Conclusions

We have presented a broad study of long-time effects based on two-dimensional simulations of CCSN. We define long-time as starting one second after the explosion and following the evolution up to around 10 s post bounce. Our study is based on three progenitors and variations of neutrino heating and rotation rates. In total, we present 46 models with 32 of them exploding. In order to be able to run so many simulations for several seconds, we have used for the neutrinos a simple leakage scheme. We are aware that the 2D and neutrino treatment simplifications are critical to the making of any quantitative conclusion. However, we have found interesting features and trends that we expect to be present in 3D detailed neutrino transport simulations. Our results indicate that the evolution during the first seconds after shock revival is not negligible, and that accretion and long-lasting downflows impact the growth of the explosion energy. The evolution during the long-time phase can be linked to initial conditions such as the rotation rate and the shock deformation. We find that neutrino-driven winds (NDWs) appear favorably in models with increased neutrino heating and rotation, and can be either long-lasting (stable) or short lived (unstable). Improved simulations following the evolution after the explosion are required to understand CCSN and the connection to observables.

During the explosion phase, both rotation and increased neutrino heating impact the shock acceleration and the initial explosion energy. Rotation weakens the explosion by decreasing the mass accretion and resulting accretion luminosity, which agrees with previous studies (Fryer & Heger 2000; Buras et al. 2003; Kotake et al. 2003; Thompson et al. 2004; Marek & Janka 2009;

Summa et al. 2018; Obergaulinger & Aloy 2020). However, an increased heating factor typically leads to more powerful explosions (O'Connor & Ott 2010; Couch & O'Connor 2014; Couch & Ott 2015).

The long-time evolution is important to estimate observables such as E_{exp}, M_{ej}, and M_{PNS}. We have found that simultaneous accretion and ejection of matter can persist for several seconds after shock revival and delay the saturation of these observables. In particular, the late-time mass accretion onto the PNS is correlated to the growth of the explosion energy, and governs the directionality of explosion energy generation. Besides different progenitors, neutrino heating, and rotation strengths, we find that the shock deformation at the onset of the explosion affects the mass accretion of the following seconds. Rapidly rotating models typically explode with a less prolate deformation, suffer less from persistent downflows, and accumulate less explosion energy in the long-time phase. The amount of ejected mass during the long-time phase is larger in fast rotating than in nonrotating models. We note that the prolate/oblate shock deformations in our models are heavily biased by our 2D geometry (Müller 2015; Nakamura et al. 2015; Bruenn et al. 2016; Summa et al. 2016; O'Connor & Couch 2018; Vartanyan et al. 2018).

The occurrence of NDWs is limited in our models to simulations with the s15 progenitor and to late times ($t > 3$ s). The total time spent in NDW phases is positively correlated with both the heating factor and rotation rate. However, we also see instances of unstable NDWs and continued accretion after such phases, typically leading to a further increase of the explosion energy. The collapse of a wind is typically induced by renewed accretion from the equatorial plane, which is a fundamentally multidimensional effect. Long-time simulations in 3D are required to further investigate the NDW.

For an analysis of the nucleosynthesis in our models, we used a tracer particle scheme that we applied to all exploding simulations of the 15 $M_\odot$ progenitor. Due to our simplified neutrino treatment, we needed to correct the neutrino energies and luminosities to account for electron fractions that are consistent with modern transport schemes. We have presented the nucleosynthesis for cold trajectories that are not exposed to neutrinos as well as for hot trajectories assuming different electron fraction distributions. All trajectories produce predominately iron group elements with hot, neutrino-processed trajectories reaching elements beyond iron depending on the electron fraction. Our results are a good indication for the potential variability in the production of elements around Sr, Y, and Zr and indicate that ^{56}Ni and ^{44}Ti are mainly produced by the hot component. In the future, longer simulation times in three dimensions with detailed neutrino transport will be necessary to connect the nucleosynthesis with the astrophysical conditions (e.g., rotation, explosion energy, and the progenitor star).

ORCID iDs

A. Psaltis ● https://orcid.org/0000-0003-2197-0797
M. Reichert ● https://orcid.org/0000-0001-6653-7538
T. Kuroda ● https://orcid.org/0000-0001-5168-6792
M. Obergaulinger ● https://orcid.org/0000-0001-5664-1382
S. M. Couch ● https://orcid.org/0000-0002-5080-5996
A. Arcones ● https://orcid.org/0000-0002-6995-3032

References

Arcones, A., & Bliss, J. 2014, JPhG, 41, 044005
Arcones, A., & Janka, H.-T. 2011, A&A, 526, A160
Arcones, A., Janka, H.-T., & Scheck, L. 2007, A&A, 467, 1227
Arcones, A., & Montes, F. 2011, ApJ, 731, 5
Blondin, J. M., Gipson, E., Harris, S., & Mezzacappa, A. 2017, ApJ, 835, 170
Bollig, R., Yadav, N., Kresse, D., et al. 2021, ApJ, 915, 28
Bruenn, S. W., Lentz, E. J., Hix, W. R., et al. 2016, ApJ, 818, 123
Bruenn, S. W., Mezzacappa, A., Hix, W. R., et al. 2013, ApJL, 767, L6
Buras, R., Janka, H.-T., Rampp, M., & Kifonidis, K. 2006, A&A, 457, 281
Buras, R., Rampp, M., Janka, H.-T., & Kifonidis, K. 2003, PhRvL, 90, 241101
Burrows, A., Dessart, L., Livne, E., Ott, C. D., & Murphy, J. 2007, ApJ, 664, 416
Burrows, A., Radice, D., & Vartanyan, D. 2019, MNRAS, 485, 3153
Burrows, A., & Vartanyan, D. 2021, Natur, 589, 29
Cabezón, R. M., Pan, K.-C., Liebendörfer, M., et al. 2018, A&A, 619, A118
Couch, S. M., Graziani, C., & Flocke, N. 2013, ApJ, 778, 181
Couch, S. M., & O'Connor, E. 2014, ApJ, 785, 123
Couch, S. M., & Ott, C. D. 2015, ApJ, 799, 5
Couch, S. M., Warren, M. L., & O'Connor, E. P. 2020, ApJ, 890, 127
Curtis, S., Ebinger, K., Fröhlich, C., et al. 2019, ApJ, 870, 2
Cyburt, R. H., Amthor, A. M., Ferguson, R., et al. 2010, ApJS, 189, 240
Dessart, L., Ott, C. D., Burrows, A., Rosswog, S., & Livne, E. 2009, ApJ, 690, 1681
Dubey, A., Daley, C., ZuHone, J., et al. 2012, ApJS, 201, 27
Dubey, A., Reid, L. B., Weide, K., et al. 2009, ParC, 35, 512
Ebinger, K., Curtis, S., Fröhlich, C., et al. 2019, ApJ, 870, 1
Ebinger, K., Curtis, S., Ghosh, S., et al. 2020, ApJ, 888, 91
Eichler, M., Nakamura, K., Takiwaki, T., et al. 2018, J. Phys. G Nucl. Part. Phys, 45, 014001
Ertl, T., Janka, H.-T., Woosley, S. E., Sukhbold, T., & Ugliano, M. 2016, ApJ, 818, 124
Fröhlich, C., Hauser, P., Liebendörfer, M., et al. 2006, ApJ, 637, 415
Fryer, C. L., & Heger, A. 2000, ApJ, 541, 1033
Fryxell, B., Olson, K., Ricker, P., et al. 2000, ApJS, 131, 273
Fujimoto, S.-i., & Nagakura, H. 2019, MNRAS, 488, L114
Fujimoto, S.-i., & Nagakura, H. 2021, MNRAS, 502, 2319
Glas, R., Janka, H. T., Melson, T., Stockinger, G., & Just, O. 2019a, ApJ, 881, 36
Glas, R., Just, O., Janka, H.-T., & Obergaulinger, M. 2019b, ApJ, 873, 45
Harris, J. A., Hix, W. R., Chertkow, M. A., et al. 2017, ApJ, 843, 2

Heger, A., Woosley, S. E., & Spruit, H. C. 2005, ApJ, 626, 350
Iwakami, W., Okawa, H., Nagakura, H., et al. 2020, ApJ, 903, 82
Janka, H.-T. 2012, ARNPS, 62, 407
Janka, H.-T., Melson, T., & Summa, A. 2016, ARNPS, 66, 341
Just, O., Bollig, R., Janka, H. T., et al. 2018, MNRAS, 481, 4786
Just, O., Obergaulinger, M., & Janka, H. T. 2015, MNRAS, 453, 3386
Kotake, K., Sumiyoshi, K., Yamada, S., et al. 2012, PTEP, 2012, 01A301
Kotake, K., Takiwaki, T., Fischer, T., Nakamura, K., & Martínez-Pinedo, G. 2018, ApJ, 853, 170
Kotake, K., Yamada, S., & Sato, K. 2003, ApJ, 595, 304
Kuroda, T., Arcones, A., Takiwaki, T., & Kotake, K. 2020, ApJ, 896, 102
Kuroda, T., Takiwaki, T., & Kotake, K. 2014, PhRvD, 89, 044011
Kuroda, T., Takiwaki, T., & Kotake, K. 2016, ApJS, 222, 20
Langanke, K., & Kolbe, E. 2001, ADNDT, 79, 293
Langanke, K., & Martínez-Pinedo, G. 2001, ADNDT, 79, 1
Lattimer, J. M., & Swesty, D. F. 1991, NuPhA, 535, 331
LeBlanc, J. M., & Wilson, J. R. 1970, ApJ, 161, 541
Liebendörfer, M. 2005, ApJ, 633, 1042
Liebendörfer, M., Rampp, M., Janka, H. T., & Mezzacappa, A. 2005, ApJ, 620, 840
MacNeice, P., Olson, K. M., Mobarry, C., de Fainchtein, R., & Packer, C. 2000, CoPhC, 126, 330
Marek, A., & Janka, H.-T. 2009, ApJ, 694, 664
Mösta, P., Richers, S., Ott, C. D., et al. 2014, ApJL, 785, L29
Müller, B. 2015, MNRAS, 453, 287
Müller, B. 2019, ARNPS, 69, 253
Müller, B., Gay, D. W., Heger, A., Tauris, T. M., & Sim, S. A. 2018, MNRAS, 479, 3675
Müller, B., Heger, A., Liptai, D., & Cameron, J. B. 2016, MNRAS, 460, 742
Müller, B., Melson, T., Heger, A., & Janka, H.-T. 2017, MNRAS, 472, 491
Müller, B., Tauris, T. M., Heger, A., et al. 2019, MNRAS, 484, 3307
Müller, E., Rampp, M., Buras, R., Janka, H. T., & Shoemaker, D. H. 2004, ApJ, 603, 221
Nagakura, H., Burrows, A., Radice, D., & Vartanyan, D. 2019a, MNRAS, 490, 4622
Nagakura, H., Burrows, A., & Vartanyan, D. 2021, MNRAS, 506, 1462
Nagakura, H., Sumiyoshi, K., & Yamada, S. 2019b, ApJL, 880, L28
Nagataki, S., Shimizu, T. M., & Sato, K. 1998, ApJ, 495, 413
Nakamura, K., Horiuchi, S., Tanaka, M., et al. 2016, MNRAS, 461, 3296
Nakamura, K., Kuroda, T., Takiwaki, T., & Kotake, K. 2014, ApJ, 793, 45
Nakamura, K., Takiwaki, T., Kuroda, T., & Kotake, K. 2015, PASJ, 67, 107
Nishimura, N., Takiwaki, T., & Thielemann, F.-K. 2015, ApJ, 810, 109
Nomoto, K., Tominaga, N., Umeda, H., Kobayashi, C., & Maeda, K. 2006, NuPhA, 777, 424
Obergaulinger, M., & Aloy, M. Á. 2020, MNRAS, 492, 4613
O'Connor, E. 2015, ApJS, 219, 24
O'Connor, E., & Ott, C. D. 2010, CQGra, 27, 114103
O'Connor, E., & Ott, C. D. 2011, ApJ, 730, 70
O'Connor, E. P., & Couch, S. M. 2018, ApJ, 854, 63
Ott, C. D., Burrows, A., Thompson, T. A., Livne, E., & Walder, R. 2006, ApJL, 164, 130
Pan, K.-C., Liebendörfer, M., Hempel, M., & Thielemann, F.-K. 2016, ApJ, 817, 72
Pan, K.-C., Mattes, C., O'Connor, E. P., et al. 2019, J. Phys. G Nucl. Part. Phys., 46, 014001
Pejcha, O., & Thompson, T. A. 2015, ApJ, 801, 90
Perego, A., Hempel, M., Fröhlich, C., et al. 2015, ApJ, 806, 275
Powell, J., & Müller, B. 2020, MNRAS, 494, 4665
Qian, Y. Z., & Woosley, S. E. 1996, ApJ, 471, 331
Reichert, M., Obergaulinger, M., Eichler, M., Aloy, M. Á., & Arcones, A. 2021, MNRAS, 501, 5733
Scheck, L., Kifonidis, K., Janka, H.-T., & Müller, E. 2006, A&A, 457, 963
Sieverding, A., Müller, B., & Qian, Y. Z. 2020, ApJ, 904, 163
Stockinger, G., Janka, H. T., Kresse, D., et al. 2020, MNRAS, 496, 2039
Sukhbold, T., Ertl, T., Woosley, S. E., Brown, J. M., & Janka, H.-T. 2016, ApJ, 821, 38
Summa, A., Hanke, F., Janka, H.-T., et al. 2016, ApJ, 825, 6
Summa, A., Janka, H.-T., Melson, T., & Marek, A. 2018, ApJ, 852, 28
Suwa, Y., Kotake, K., Takiwaki, T., et al. 2010, PASJ, 62, L49
Suwa, Y., Kotake, K., Takiwaki, T., Liebendörfer, M., & Sato, K. 2011, ApJ, 738, 165
Takiwaki, T., Kotake, K., & Suwa, Y. 2016, MNRAS, 461, L112
Thielemann, F.-K., Nomoto, K., & Hashimoto, M.-A. 1996, ApJ, 460, 408
Thompson, T. A., Chang, P., & Quataert, E. 2004, ApJ, 611, 380
Timmes, F. X., & Arnett, D. 1999, ApJS, 125, 277
Timmes, F. X., & Swesty, F. D. 2000, ApJS, 126, 501

Ugliano, M., Janka, H.-T., Marek, A., & Arcones, A. 2012, ApJ, 757, 69
Vartanyan, D., Burrows, A., & Radice, D. 2019a, MNRAS, 489, 2227
Vartanyan, D., Burrows, A., Radice, D., Skinner, M. A., & Dolence, J. 2018,
    MNRAS, 477, 3091
Vartanyan, D., Burrows, A., Radice, D., Skinner, M. A., & Dolence, J. 2019b,
    MNRAS, 482, 351

Wanajo, S., Müller, B., Janka, H.-T., & Heger, A. 2018, ApJ, 852, 40
Winteler, C. 2011, PhD Thesis, Univ. of Basel
Winteler, C., Käppeli, R., Perego, A., et al. 2012, ApJL, 750, L22
Wongwathanarat, A., Müller, E., & Janka, H.-T. 2015, A&A, 577, A48
Woosley, S. E., Heger, A., & Weaver, T. A. 2002, RvMP, 74, 1015
Woosley, S. E., & Weaver, T. A. 1995, ApJS, 101, 181